3D visual-based tension control in strip-like deformable objects using a catenary model

N. Roca Filella, Adrien Koessler, B.C. Bouzgarrou, Juan Antonio Corrales Ramon

2022 IEEE/RSJ International Conference on Intelligent Robots and Systems (IROS 2022)
October 23-27, 2022, Kyoto, Japan

3D visual-based tension control in strip-like deformable objects using a catenary model

N. Roca Filella[1], A. Koessler[1,2], B.C. Bouzgarrou[1] and J.-A. Corrales Ramon[3]

***Abstract*— In recent years, there has been a growing interest in robotic manipulation of deformable objects. In order to perform certain tasks, the robot must control the shape of the object while taking care not to apply excessive stresses so as not to deform it irreversibly. This is the case when extracting elasto-plastic objects in strips from an industrial reel. In order to control the mechanical stresses within the object, we propose a vision-based control scheme to minimize tension by regulating the angular velocity of a motorized reel on which they are wound. In this paper, we propose a method, based on a catenary model and visual feedback from a low-cost RGB-D camera, to estimate the tension distribution along a rubber strip. Thus, the control strategy aims to achieve a desired tension value by varying the length of the suspended portion of the manipulated strip. Simulation and experimental results validate the proposed approach for strip-like objects of various dimensions.**

I. Introduction

Deformation control of soft objects like fabrics, foam and other elastic bodies is now a matter of ongoing research in the field of robotic manipulation [1]. Their deformation is generally modeled by introducing new degrees of freedom (DOF), which makes control more challenging. Perception based on vision, tactile or multi-modal sensing is hence used to estimate these additional DOFs, which represent the state of deformation of the object [2]. That allows closing the control loop and ensures task achievement. Some methods, known as *model-free* methods, do not require a model and are based on perceived data, like position, angle, or shape, decorrelated from the object parameters. In [3] visual data are collected to estimate locally the deformation Jacobian matrix, avoiding any model identification step. The work of [4] uses both visual and force sensor for robotic cutting of deformable objects. These methods avoid modeling the dynamics of the objects in its environment but often need a lot of input data if they are based on supervised learning and are not very generalizable. Another solution is to use a model that facilitates the description of the object. These models can be classified in two main categories based on their complexity.

Physical-based models: Based on mechanical equations, they are as close as possible to reality. The two main models are Finite Element (FE) and Mass-Spring-Damper models. For instance, we can mention the research of [5] and [6], which use such models in generic manipulation cases.In [7] the desired actuator motions are computed in real-time as an inverse solution of a FEM problem. The gripper's configuration is coupled to a FE model in [8] to perform an open-loop shape control. These methods are physically relevant and useful for changeable object shapes and material behaviours. However, these physical models are not suitable for varying mass objects (such as a strip that is unrolled from a reel) and often requires a lot of nodes which is resource-consuming. Recently, the work of [9] used low node count FE models for shape control to reduce the computational cost.

Geometry-based models: To overcome these drawbacks, non-physical models can be used. In these approaches, deformation is generally modeled using explicit mathematical formulations of object shape, which allow fast computations within a control loop. The deformation is estimated using geometrical features like positions, curvatures or surfaces. In [10] a simple approach to track elongated extended objects using Bézier curve is introduced. This algorithm is fast and robust even with partially occluded target. The deformation of the surface object is estimated in [11] using non-uniform rational basis splines approximation with a RGB-D camera. A shape control of isometrically deforming objects with 2D camera is proposed in [12]. These methods show a good balance between computational cost and accuracy. However, most of these approaches do not take material properties into account and only guarantee good results for the controlled features.

For a deformable object, this is a crucial point in several applications because stress must not increase beyond the elastic limit, so that the material does not undergo a plastic deformation. In this paper, we explore the field of tension control which consists in setting and maintaining a desired tension in an object to prevent damaging it while manipulating it. The research of [13] and [14] exploits and validates the use of a model for strip-like deformable objects, based on a catenary curve. This geometry-based model can be considered at the intersection of the two previous methods, as it gives information on the tension in the object. These works could be coupled to those of [15] to replace expensive force sensor by a vision sensor in [13], but also in [16] where a robot takes a deformable belt out of a bobbin using a F/T sensor.

Proposed contributions: In this work, we introduce a visual-based tension control scheme for strip-like deformable objects, whose one end is grasped by a robot and the other

[1] Université Clermont Auvergne, Clermont Auvergne INP, CNRS, Institut Pascal, F-63000 Clermont-Ferrand, France {firstname.lastname}@sigma-clermont.fr

[2] Université de Lorraine, Arts et Metiers Institute of Technology, LCFC, HESAM Université, F-57070 Metz, France

[3] Centro Singular de Investigación en Tecnoloxías Intelixentes (CiTIUS), Universidade de Santiago de Compostela, 15782, Santiago de Compostela, SPAIN {firstname.lastname}@usc.es

978-1-6654-7927-1/22/$31.00 ©2022 IEEE

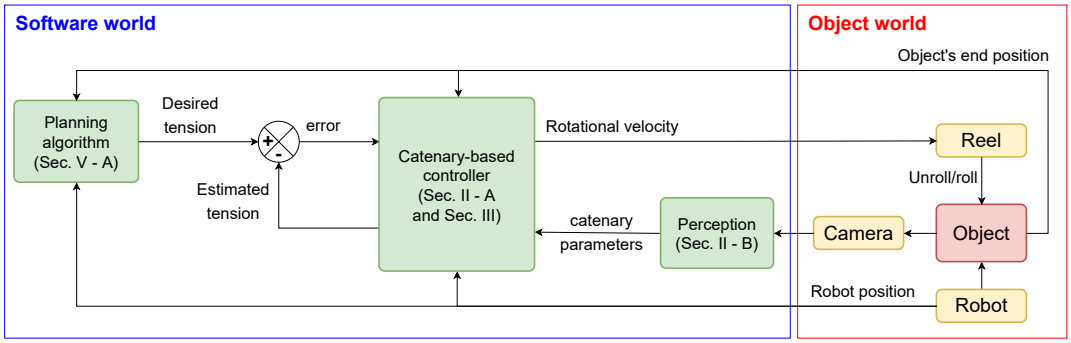

Fig. 1. Control logic block diagram of our proposed method for visual-based tension control scheme.

is wound onto a reel. Using a low-cost RGB-D camera and a 3D catenary model, the deformation state is estimated without any contact by partial observation of the object. A closed-loop tension control scheme managing the rotation of the reel is then proposed to vary the length of linear objects in real-time. Experiments regarding our use case are performed in simulation, then on the real robotic system. A simplified control logic block diagram is shown in Fig. 1.

II. Tension Estimation by Vision

In this section, a catenary-based model is introduced. We use a method to fit strip-like deformable objects in 3D space and estimate the tension in the object. We evaluate the quality of tension estimation in comparison with a force sensor.

A. Catenary-based model

A catenary is the curve that an idealized hanging chain or cable assumes under its own weight (uniformly distributed) when supported only at its ends [17]. The use of catenaries was encouraged by the fact that this model gives useful information on tension in the object. The model is well suited for strip-like deformable objects, considering that the thickness d_{obj} and the width of a strip-like deformable object are very small when compared to its length L, and assuming zero bending stiffness. It is also assumed that no torsional stress is applied, which allows us to reduce the representation in a plane.

Let $O(\vec{x},\vec{z})$ be the global frame in 2D space, E_1 and E_2 the ends of the catenary, $P_i(x_i,z_i)$ any point in the curve and $P_{low}(x_{low},z_{low})$ the lowest point of the curve, as depicted in Fig. 2.

The height $h_i = z_i - z_{low}$ represents the sag at point P_i, and l_i is the length of the segment of curve, from P_{low} to P_i. At any point, the following catenary equation is verified [18]:

$$z = z_{low} + c\left(\cosh\left(\frac{x - x_{low}}{c}\right) - 1\right) \tag{1}$$

where $c = T_{H,i}/\mu g$ is the catenary constant depending on the shape of the strip. μ is the mass per unit length and $g = 9.81\ m\cdot s^{-2}$ is the acceleration of gravity. This introduces $T_{H,i}$, the horizontal component of the total tension $T_{T,i}$ at

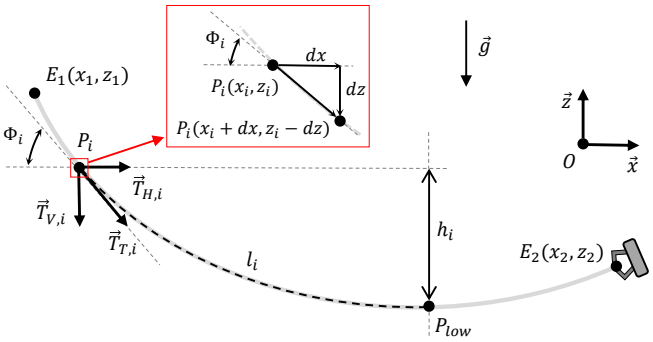

Fig. 2. Representation of a catenary in the 2D space.

point P_i, as follows:

$$T_{H,i} = \mu g c. \tag{2}$$

According to Fig. 1, the vertical component is defined as $T_{V,i} = T_{H,i}\tan\Phi_i$ where Φ_i is the tangential angle formed by the catenary at point P_i. We assume that for a infinitely small change in x, dx, the infinitely small change in z is given by $dz{=}dx\tan\Phi_i$ and we have

$$\begin{aligned} T_{V,i} &= T_{H,i}\sinh\left(\frac{x_i - x_{low}}{c}\right) \\ &= \mu g l_i \end{aligned} \tag{3}$$

where, by definition and for $x_i < x_{low}$,

$$\begin{aligned} l_i &= \int_{x_i}^{x_{low}} \sqrt{1 + \left(\frac{dz}{dx}\right)^2}\, dx \\ &= -c\sinh\left(\frac{x_i - x_{low}}{c}\right). \end{aligned} \tag{4}$$

Considering that $T_{T,i} = \sqrt{{T_{H,i}}^2 + {T_{V,i}}^2}$ and (1) , we have

$$\begin{aligned} T_{T,i} &= \mu g c\sqrt{1 + \sinh^2\left(\frac{x_i - x_{low}}{c}\right)} \\ &= \mu g c\left(\frac{z_i - z_{low} + c}{c}\right) \\ &= \mu g\,(c + h_i) \end{aligned} \tag{5}$$

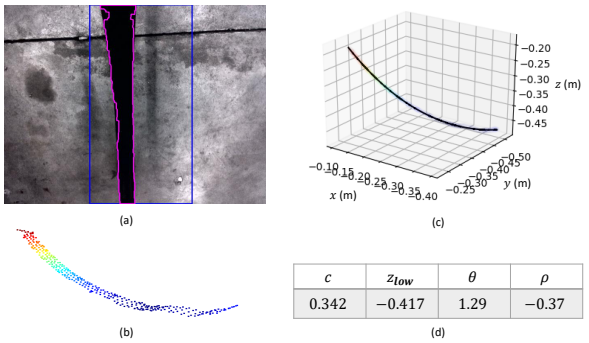

c	z_{low}	θ	ρ
0.342	−0.417	1.29	−0.37

Fig. 3. (a) object detection in color image, (b) down-sampled 3D point cloud, (c) fitted catenary curve and (d) identified parameters.

As we can see, the total tension depends only on three parameters of the catenary, μ, c and z_{low}, no matter the value of x_{low}. From now, we consider changing it to a 3D object being projected.

A model of 3D catenary is proposed in [19]. Its expression at any point in the 3D camera frame $C(\vec{x}\prime,\vec{y}\prime,\vec{z})$ is as follows:

$$z = z_{low} + c\left(\cosh\left(\frac{x'\cos\theta - y'\sin\theta - \rho\sin\theta}{c}\right) - 1\right) \quad (6)$$

where θ is the azimuth and ρ is the distance from the origin when the 3D catenary is projected into the $x'-y'$ plane as a straight line. For a transformation from 3D camera frame to 2D object frame, we use the variable substitution introduced in [19]: $x = x'\cos\theta - y'\sin\theta$ and $x_{low} = \rho\sin\theta$.

B. Object detection and 3D curve fitting

An RGB-D camera is positioned above the target object. After the acquisition of the image, a depth thresholding is processed to extract the foreground. A color segmentation is then applied, and the relevant point cloud is extracted. To reduce the computing cost, a 3D down-sampling is performed. Finally, to eliminate noise in the detection, a 3D clustering is applied using DB-SCAN algorithm [20].

A 3D curve fitting method using non-linear least squares is then implemented to fit the function to the point cloud. It uses a Trust Region Reflective algorithm [21] which is ideal for a bound-constrained minimization problem. Fig. 3 (a) shows that the strip is well detected in color image and Fig. 3 (b) shows the point cloud before down-sampling and clustering. Despite the significant depth noise, the identified curve correctly fits to the point cloud in Fig. 3 (c). In Fig. 3 (d) the identified parameters are shown. Finally, the results highlight that the proposed method does not need full object perception, as seen in Fig. 3 (a) where both ends are not in the color image.

C. Validation of the visual estimation

Once the parameters z_{low}, c, ρ and θ are estimated, the strip-like object is reduced to a curve with a negligible width, so (2), (3) and (5) can be used to estimate the tension.

We now make a comparison between the tension estimated using the visual method and the one measured by two accurate force sensors (s-type load cells) with an announced accuracy of ± 0.1 percent for 10 N. We use the three objects of Table I of length $l = 0.90$ and in four different cases: $|x_1 - x_2| = \{0.74, 0.79, 0.84, 0.89\}$. We compute the mean values and standard deviations (SD) and the results are shown in Table II. Even though small differences can be observed between the two methods, our method is suitable for low tension estimation.

Strip-like object	$\mu\ kg\cdot m^{-1}$
1	0.132
2	0.106
3	0.037

TABLE I

MASS PER UNIT LENGTH OF THE MANIPULATED OBJECTS.

	case 1		case 2		case 3		case 4	
Object	mean	SD	mean	SD	mean	SD	mean	SD
1 (force)	0.77	0.001	0.88	0.001	1.12	0.001	3.48	0.011
1 (vision)	0.76	0.004	0.86	0.006	1.16	0.014	3.22	0.212
2 (force)	0.61	0.001	0.71	0.001	0.98	0.001	2.41	0.009
2 (vision)	0.61	0.003	0.70	0.008	0.99	0.019	2.45	0.159
3 (force)	0.22	0.001	0.26	0.001	0.36	0.001	1.20	0.011
3 (vision)	0.21	0.001	0.24	0.001	0.30	0.004	0.82	0.090

TABLE II

COMPARISON OF MEAN VALUE AND SD (IN N).

For case 4, the object remains flat, even after being more stretched and our method reaches its limit of validity. In that case, a Force/Torque sensor can be used as an add-on tool for the robot. Fig. 4 now shows a comparison between the horizontal tension measured by a Robotiq FT300 F/T sensor and the tension estimated with our method. We manually rotate the reel to vary the length of the object during 50 acquisitions. Our proposed visual method seems to be more stable thanks to the fitting step which smooth the values of tension. When the object is flat, it becomes impossible to estimate the correct value of parameters c with our visual method, therefore we impose a maximum threshold for this value and the F/T sensor gives better results.

In conclusion, the catenary model is well adapted especially when the object does not become flat. The precision and efficiency of this novel perception method enables loop closure for tension control. We will synthesize such a controller, with an approach based on the formerly introduced model.

III. CLOSED-LOOP TENSION CONTROL SCHEME

In this section, we present the control scheme to manipulate the strip-like object using the previous visual feedback. The purpose is to control the angular velocity of the reel ω to vary the length l of the object.

A. Tension control law synthesis

We assume that positions at both ends are known and that E_1 is fixed. It is, and stays, the highest point of the curve

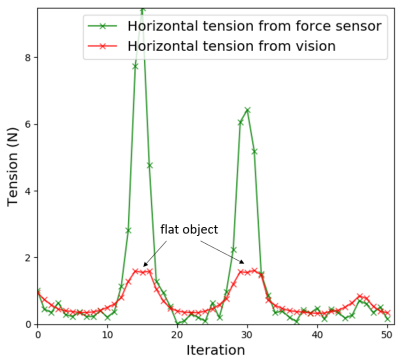

Fig. 4. Comparison of horizontal tension measured using the F/T sensor (green) and the visual sensors (red).

during all the manipulation. This assumption implies that, according to (5), the tension has a global maximum at this point, as $h_1 = max(h_i)$. E_2 is grasped by the end-effector of the robot. To simplify the notation in the following, both T_{H,x_1} and T_{T,x_1} are represented by T. We denote T^d the desired tension and define $\dot{T}$ as:

$$\dot{T} = \frac{dT}{dl}\dot{l} \tag{7}$$

where $l = l_1 - l_2$. The aim is to exponentially decrease the error $e = T^d - T$ towards zero with the following control law based on a first-order dynamic behavior:

$$\dot{e} + Ke = 0 \tag{8}$$

with $K > 0$. Merging (7) and (8), we obtain the following control law on $\dot{l}$ to ensure that the tension converges towards the desired tension:

$$\dot{l} = \frac{dl}{dT}\left(u + \dot{T^d}\right) \tag{9}$$

with $u = Ke$. This leads to a rotational control of the reel though $\omega = \dot{l}/R$, where R is the radius of the reel. After that, the length of the strip-like object is modified, and so the catenary too. We consider the desired tension remaining constant over time, hence $\dot{T}^d = 0$.

By now, the aim is to define the derivative of T with respect to l, i.e. determine the influence of a small variation of the length on the tension.

B. Control of the horizontal component

Controlling the horizontal component of the tension at E_1 allows a control at any point of the object, as $dT_{H,i}/dx = 0$. The derivative of $T_{H,1}$ with respect to l is defined as follows:

$$\frac{dT_{H,1}}{dl} = \mu g \frac{dc}{dl}. \tag{10}$$

We now want to express dc/dl. By subtracting (1) at points E_1 and E_2, we obtain

$$\begin{aligned} z_2 - z_1 &= c\left(\cosh\left(\frac{x_2 - x_{low}}{c}\right) - \cosh\left(\frac{x_1 - x_{low}}{c}\right)\right) \\ &= 2c\sinh\left(\frac{x_1 + x_2 - 2x_{low}}{2c}\right)\sinh(A) \end{aligned} \tag{11}$$

where $A = (x_2 - x_1)/2c$. Using (4), we have

$$\begin{aligned} l &= c\left(\sinh\left(\frac{x_2 - x_{low}}{c}\right) - \sinh\left(\frac{x_1 - x_{low}}{c}\right)\right) \\ &= 2c\cosh\left(\frac{x_1 + x_2 - 2x_{low}}{2c}\right)\sinh(A). \end{aligned} \tag{12}$$

If we divide (11) by (12) for $l \neq 0$, we obtain

$$\frac{x_1 + x_2 - 2x_{low}}{2c} = \operatorname{arctanh}\left(\frac{z_2 - z_1}{l}\right). \tag{13}$$

Integrating (13) into (12), we finally get

$$\frac{l}{\cosh\left(\operatorname{arctanh}\left(\frac{z_2 - z_1}{l}\right)\right)} = 2c\sinh(A). \tag{14}$$

One can verify that the left side of (14), denoted f_1, depends on l and the right side, denoted f_2, depends on c. We hence have the following derivative of c with respect to l:

$$\frac{dc}{dl} = \frac{df_1}{dl}\frac{dc}{df_2} \tag{15}$$

where, by derivation,

$$\frac{df_1}{dl} = \frac{l}{\sqrt{l - (z_2 - z_1)}\sqrt{l + (z_2 - z_1)}} \tag{16}$$

and

$$\frac{df_2}{dc} = 2\sinh(A) - (2A)\cosh(A). \tag{17}$$

From equation (3), we understand that the longer the object is, the higher the vertical tension is. That means that even if the object is sagging, it can be stretched at its ends under its weight. The vertical tension hence becomes impossible to ignore in our computations and we will now focus on the control of the total tension.

C. Control of the total tension

We now express the derivative of $T_{T,1}$ with regards to l. From (5), we obtain:

$$\frac{dT_{T,1}}{dl} = \mu g\left(\frac{dc}{dl} + \frac{dh_1}{dl}\right). \tag{18}$$

To express the derivative of h_1 with respect to l, we use the following decomposition:

$$\frac{dh_1}{dl} = \frac{dh_1}{dc}\frac{dc}{dl} \tag{19}$$

Using (1) and (14) into h_1, we obtain:

$$\begin{aligned} h_1 &= z_1 - z_{low} \\ &= c(\cosh(B) - 1) \end{aligned} \tag{20}$$

where $B = \dfrac{x_1 - x_2}{2c} + \operatorname{arctanh}\left(\dfrac{z_2 - z_1}{l}\right)$. By derivation, we have:

$$\begin{aligned} \frac{dh_1}{dc} &= \cosh(B) - 1 - c\sinh(B) \\ &\cdot\left(\frac{dl}{dc}\left(\frac{z_2 - z_1}{l^2 - (z_2 - z_1)^2}\right) + \frac{x_1 - x_2}{2c^2}\right) \end{aligned} \tag{21}$$

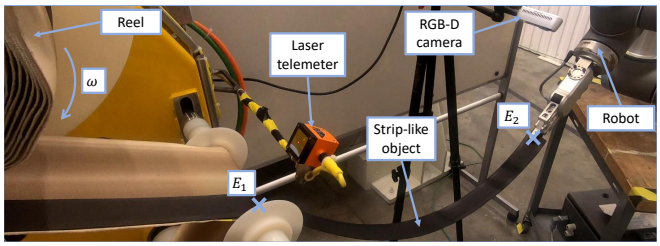

Fig. 5. Picture of the experimental setup.

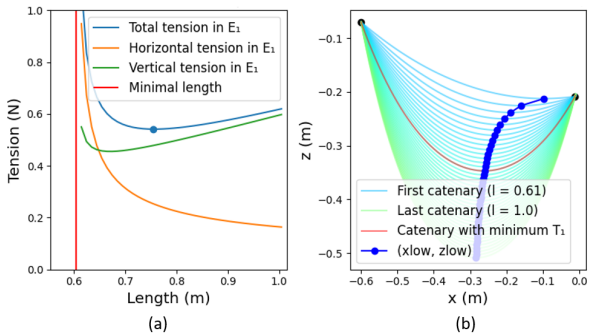

Fig. 6. (a) tensions according to l, (b) evolution of the catenary while l is increasing.

Finally, replacing (21) into (19), we have an equation for (18) and we can integrate it into (9) to formulate a law that controls the total tension, and not only the horizontal component. From now on, we consider the total tension as the servoed variable and drop the subscript, so that $T_{T,1}$ is now referred to as T_1 in the following experimental analysis.

IV. Setup of the Application

The simulation and the experimentation will be firstly focused on the rubber strip-like object 2. As shown in Fig. 5, an Intel RealSense D435 RGB-D camera is placed at $C(0,0)$. The point E_2 is grasped and driven by a Universal Robots UR10 robot while $E_1(-0.570,-0.120)$ is held fixed during the manipulation. The rotating reel is motorized to adjust T_1. This first experiment **Exp. 1** is divided in three phases:

- **Phase 1**: For 5 s, the robot stays in A so that the tension settles around the initial desired tension.
- **Phase 2**: The robot drives E_2 from $A(-0.018,-0.258)$ to $B(0.197,-0.511)$ into the $x-z$ plane in 5 s seconds at an average velocity of $v = 0.062\ m.s^{-1}$.
- **Phase 3**: The robot stops for 5 seconds so that the tension settles around the final desired tension

V. Simulation Results

As the control law was already established, the choice of the desired tension remains to be determined. But looking at the equations, the choice of a reachable tension is not trivial. In this section, we perform simulation to find adequate values for desired tensions. Once this is done, we introduce the tuning process and evaluate the impact of disturbances on the control law, such as robot motion and radius variation.

A. Trajectory planning of the desired tension

For a given position of E_1 and E_2, it is possible to find c given the length l by solving numerically the folowing equation:

$$z_2 - z_1 - 2c\sinh(A+B)\sinh(A) = 0 \tag{22}$$

found using (11) and (13). We likewise find x_{low} solving numerically (11). Now that c and x_{low} are known, the tension components according to l are presented in Fig. 6 (a) for a given position and the evolution of the catenary can be seen in Fig. 6 (b). We notice that the horizontal tension (in orange) decreases with l increasing, while the vertical tension (in green) increases. They hence have opposite behaviours while changing the length. It is then difficult to predict that of the total tension. To overcome this, we propose an on-line trajectory planning method for T_1^d. The Algorithm 1 is dedicated to minimize $T_1(l)$ (i.e. to find the minimum of the blue curve) so that, at each time, $T_1^d = \min(T_1(l))$. As the robot has soft acceleration and deceleration, a smooth variation of the desired tension is planned.

Algorithm 1: find T_1^d, the minimum of T_1

Initialisation: $T_1^d \leftarrow 10$; $dl \leftarrow 0.05$; $l \leftarrow ||\vec{E_1E_2}|| + dl$; $c_0 \leftarrow 0.1$; $x_{low,0} \leftarrow (x_1+x_2)/2$;
while $l \leq 3$ **do**
  $c \leftarrow findc(l,x_1,x_2,z_1,z_2,c_0)$ solving numerically (22);
  $x_{low} \leftarrow findx_{low}(x_1,x_2,z_1,z_2,c,x_{low,0})$ solving numerically (11);
  $T_1 \leftarrow computeTension(c,x_1,x_{low})$ using (5);
  if $T_1 \leq T_1^d$ **then**
    $T_1^d \leftarrow T_1$;
  end
  $l \leftarrow l + dl$; $c_0 \leftarrow c$; $x_{low,0} \leftarrow x_{low}$;
end

B. Proportional gain tuning

To evaluate the impact of K in the control law, we choose four different values: $K = \{1,3,6,9\}$. The results of tension estimation and output control are presented in Fig. 7. The error exponentially converges toward zero during phases 1 and 3, as expected. Regarding phase 2, the robot motion causes a delay, that $K = 1$ cannot compensate. The high gain $K = 9$ involves undesired oscillations. Finally, $K = 3$ and $K = 6$ seems to be appropriate solutions.

C. Influence of a time-dependent radius

One can see that a constant radius has been chosen in the control law. However the more the object is unwound, the smaller the radius is. The radius is indeed a time-dependent variable.

To include the thickness in the simulation, we multiply $\dot{l}$ by $(R-var)/R$ with $var = \beta.d_{obj}/2\pi$ the variation of radius

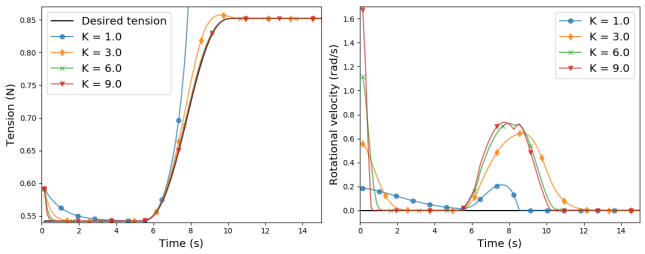

Fig. 7. Estimated tension vs. computed velocity output.

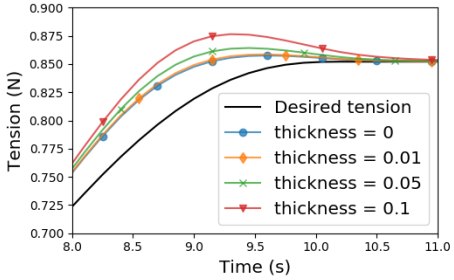

Fig. 8. Estimated tension with different thickness of the object.

and where β is the rotational angle of the reel (initially, $\beta = 0$). In Fig. 8, we compare the tension with different values for thickness of the object: $d_{obj} = \{0, 0.01, 0.05, 0.1\}$ and for $R = 0.148$. The error due to the radius variation is taken into account in the controller error when $d_{obj} \neq 0$. The final target tension is reached shortly after, because $\dot{l}$ is smaller than it should be. Despite that small difference in terms of speed of convergence, we assume that the radius could be measured off-line before each experiment.

Positive results achieved during this simulation phase encourage us to evaluate the fitting method and the proposed control law in real settings.

VI. Experimental results

This section shows the tension control on the real system described in Section IV. We present here a comparison with the simulation use case, as well as novel experiments with more varied robot arm trajectories and objects.

A. Comparison between simulation and experimental results

We performed experimental tension control for $K = \{1, 3, 6\}$ and we compare the results with the simulation results in Fig. 9. Given the measurement accuracy of our visual tension estimator, we decided to limit the output control when the robot is not moving if $|e|$ is smaller than $\varepsilon = 0.01\ N$. This solution helped our system to become more stable and to converge towards the final desired tension for $K = 3$ and $K = 6$ and the results are nearly the same as the simulation ones. As expected, $K = 1$ is not sufficient for a fast response. One can notice that the output for $K = 6$ presents some considerable oscillations.

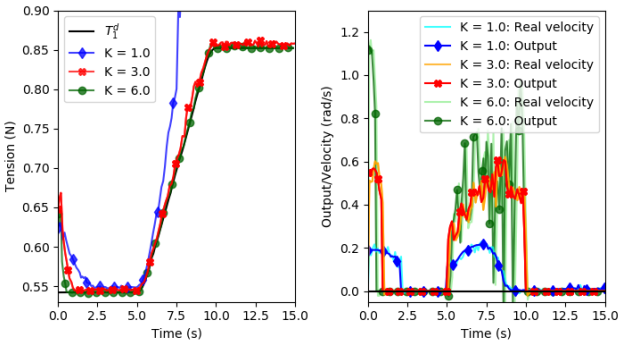

Fig. 9. Estimated tension vs. computed velocity output and real velocity.

B. Additional experiments

In this section, we propose to validate our controller in different use-cases. For each experiment, we choose $K = 3$ in accordance with previous results. Here a description for three new experiments:

- **Exp. 2**: After 5 s the robot arm follows circular trajectory (3 laps) with increasing velocity: 0.1 $m \cdot s^{-1}$ (1st lap), 0.15 $m \cdot s^{-1}$ (2nd lap) and 0.2 $m \cdot s^{-1}$ (3rd lap). The acceleration is 0.3 $m \cdot s^{-2}$.
- **Exp. 3**: The robot follows a rectangle trajectory starting at $t = 0$ s with a velocity of 0.25 $m \cdot s^{-1}$ and an acceleration of 1.2 $m \cdot s^{-2}$. It was designed to measure the impact of a bigger acceleration while the value of T_1 has not yet settled. Also, this is the experiment with the largest distance between E_1 and E_2.
- **Exp. 4**: After 5 s, the robot goes back and forth and wait for 1 s with a velocity of 1.2 $m \cdot s^{-1}$ and a acceleration of 1.2 $m \cdot s^{-2}$ (5 repetitions). Probably, the robot does not have time to reach this velocity but this experiment was designed to see how the controller reacts when faced to oscillations.

One can find the trajectory of each experiments and the results of the tension control in Fig. 10. The root mean square percentage error (RMSPE) and the maximal percentage error $e_{p,max}$ while the robot is moving are presented in Table III. The choice of a percentage error is motivated by the difference in scale between two objects. From Exp. 2, it can be seen that increasing the velocity of the robot also increases the tension overshoot. However, T_1 still converges towards the desired value once the motion is stopped. This behaviour is also observed in Exp. 3, where the initial mismatch in tension has no visible effect on the quality of tension servoing. From this, we can conclude on the efficiency of the proposed method, provided the dynamics of the robot leading the motion are not too high.

C. Instability due to dynamics

The experimental analysis has shown the viability of the proposed method. However, as the length increases a novel problem appears: the object becomes more vulnerable to oscillations caused by the variation of the output control.

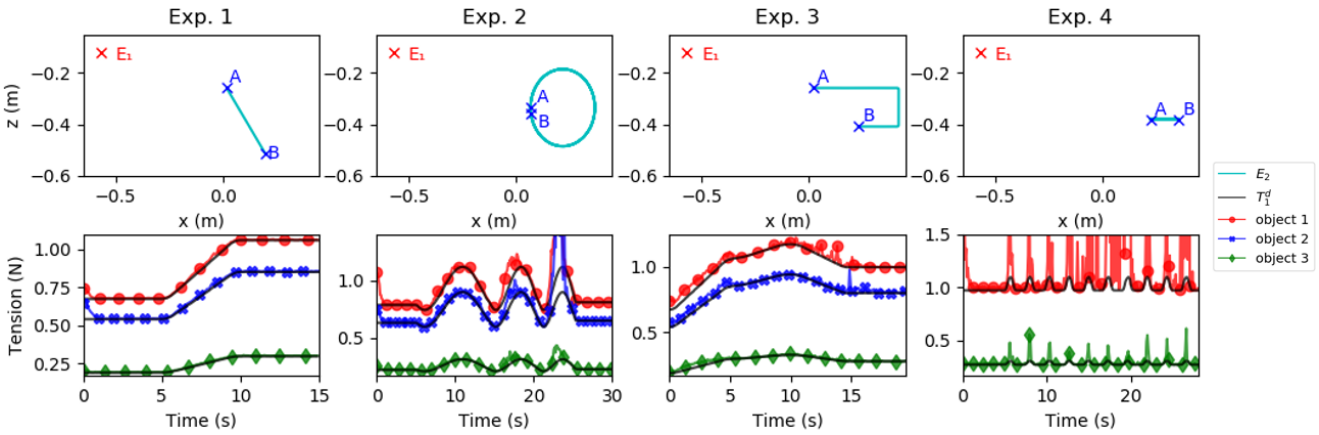

Fig. 10. Trajectory of each experiment and results of the tension control.

	Object 1		Object 2		Object 3	
Experiment	RMSPE	$e_{p,max}$	RMSPE	$e_{p,max}$	RMSPE	$e_{p,max}$
1	0.92	3.55	1.00	3.97	1.33	3.83
2 (1st lap)	1.34	7.76	1.50	7.06	1.52	7.19
2 (2nd lap)	4.36	23.41	3.24	18.68	4.49	39.65
2 (3rd lap)	14.45	111.24	20.44	157.69	7.68	51.38
3	3.98	13.4	3.20	9.93	5.49	17.21
4	405.99	2718.31	X	X	14.8	99.4

TABLE III

RMSPE AND $e_{p,max}$ FOR EACH EXPERIMENTS.

For Exp. 1-3, there was no notable difference in RMSPE depending on the object. However, in Exp. 4, the system performs way worse on the heavier object than on the lighter one. We conclude that taking dynamics into account would be a mandatory step in the future in order to deal with lengthier and heavier objects. In that precise case, the use of a FE model might be useful.

VII. Conclusion

In this work, we have proposed a closed-loop tension control for strip-like deformable objects. A 3D catenary-based model was used to estimate the internal tension of a linear deformable object pulled by a robot. The control law regulates the angular velocity of a reel onto which the object is wound, in order to vary the object length and to ensure the object is not stretched. In that way, we prevent the object from an irreversible deformation. The proposed work has been validated in simulation first. An algorithm of trajectory planning for the desired tension has been implemented and a gain tuning has been made. After that, we evaluated our controller with several trajectories of the robot and several parameters of the objects.

The proposed method gives a deformation state in real-time using a low-cost RGB-D sensor instead of a dedicated force sensor. The 3D fitting method allows an estimation despite partial observation and results in smoothed feedback. Finally, the catenary model is easy to identify, since the only relevant parameter is the mass per unit length. Experimental results have proven the capacity of the method to handle various materials successfully.

Future works will focus on strip-like deformable objects with higher thickness and significant bending stiffness. Moreover, the study of inertial effects would be necessary to control the oscillations of the strips, especially for longer objects and faster task execution.

Acknowledgements

This research made in the FACTOLAB framework has been sponsored by Michelin Tyres Manufacturer, by the French government research programs "Investissements d'Avenir" through the IDEX-ISITE initiative 16-IDEX-001 (CAP 20-25) and the IMobS3 Laboratory of Excellence (ANR-10-LABX-16-01). CIFRE 2019/0917. JACR was funded by the Spanish Ministry of Universities through a 'Beatriz Galindo' fellowship (Ref. BG20/00143) and by the Spanish Ministry of Science and Innovation through the research project PID2020-119367RB-I00.

References

[1] J. Sanchez, J. A. Corrales, B. C. Bouzgarrou, and Y. Mezouar, "Robotic manipulation and sensing of deformable objects in domestic and industrial applications: a survey," *International Journal of Robotics Research*, vol. 37, no. 7, pp. 688–716, 2018.

[2] F. Nadon, A. J. Valencia, and P. Payeur, "Multi-modal sensing and robotic manipulation of non-rigid objects: A survey," *Robotics*, vol. 7, no. 4, 2018.

[3] D. Navarro-Alarcón, Y. H. Liu, J. G. Romero, and P. Li, "Model-free visually servoed deformation control of elastic objects by robot manipulators," *IEEE Transactions on Robotics*, vol. 29, no. 6, pp. 1457–1468, 2013.

[4] P. Long, W. Khalil, and P. Martinet, "Robotic cutting of soft materials using force control and image moments," in *2014 13th International Conference on Control Automation Robotics and Vision (ICARCV)*, 2014, pp. 474–479.

[5] J. Sanchez, C. M. Mateo, J. A. Corrales, B. Bouzgarrou, and Y. Mezouar, "Online shape estimation based on tactile sensing and deformation modeling for robot manipulation," in *2018 IEEE/RSJ International Conference on Intelligent Robots and Systems (IROS)*, Oct 2018, pp. 504–511.

[6] J. Das and N. Sarkar, "Autonomous shape control of a deformable object by multiple manipulators," *Journal of Intelligent & Robotic Systems*, vol. 62, pp. 3–27, 2011.

[7] F. Ficuciello, A. Migliozzi, E. Coevoet, A. Petit, and C. Duriez, "Fem-based deformation control for dexterous manipulation of 3d soft objects," in *2018 IEEE/RSJ International Conference on Intelligent Robots and Systems (IROS)*, Oct 2018, pp. 4007–4013.

[8] S. Duenser, J. M. Bern, R. Poranne, and S. Coros, "Interactive robotic manipulation of elastic objects," in *2018 IEEE/RSJ International Conference on Intelligent Robots and Systems (IROS)*, 2018, pp. 3476–3481.

[9] A. Koessler, N. R. Filella, B. Bouzgarrou, L. Lequièvre, and J.-A. C. Ramon, "An efficient approach to closed-loop shape control of deformable objects using finite element models," in *2021 IEEE International Conference on Robotics and Automation (ICRA)*, 2021, pp. 1637–1643.

[10] A. Zea, F. Faion, and U. D. Hanebeck, "Tracking elongated extended objects using splines," in *2016 19th International Conference on Information Fusion (FUSION)*, July 2016, pp. 612–619.

[11] A. Jordt and R. Koch, "Fast tracking of deformable objects in depth and colour video." in *BMVC*, 2011, pp. 1–11.

[12] M. Aranda, J. Antonio Corrales Ramon, Y. Mezouar, A. Bartoli, and E. Özgür, "Monocular visual shape tracking and servoing for isometrically deforming objects," in *2020 IEEE/RSJ International Conference on Intelligent Robots and Systems (IROS)*, 2020, pp. 7542–7549.

[13] S. Flixeder, T. Glück, and A. Kugi, "Force-based cooperative handling and lay-up of deformable materials: Mechatronic design, modeling, and control of a demonstrator," *Mechatronics*, vol. 47, pp. 246–261, 2017.

[14] X. Xiao, Y. Fan, J. Dufek, and R. Murphy, "Indoor uav localization using a tether," in *2018 IEEE International Symposium on Safety, Security, and Rescue Robotics (SSRR)*, Aug 2018, pp. 1–6.

[15] M. Laranjeira, C. Dune, and V. Hugel, "Embedded visual detection and shape identification of underwater umbilical for vehicle positioning," in *OCEANS 2019 - Marseille*, June 2019, pp. 1–9.

[16] Y. QIN, A. Escande, A. Tanguy, and E. Yoshida, "Take a long deformable belt out of a bobbin by humanoid robot," *The Proceedings of JSME annual Conference on Robotics and Mechatronics (Robomec)*, vol. 2020, pp. 1P1–B04, 11 2020.

[17] R. Yates, *A Handbook on Curves and Their Properties*, Jan 1952, ch. Catenary, pp. 12–14.

[18] S. J. Sugden, "Construction of transmission line catenary from survey data," *Applied Mathematical Modelling*, vol. 18, no. 5, pp. 274–280, 1994.

[19] T. Chan and D. Lichti, "3d catenary curve fitting for geometric calibration," *ISPRS - International Archives of the Photogrammetry, Remote Sensing and Spatial Information Sciences*, vol. XXXVIII-5/W12, pp. 259–264, May 2012.

[20] M. Ester, H.-P. Kriegel, J. Sander, and X. Xu, "A density-based algorithm for discovering clusters in large spatial databases with noise," in *Proceedings of the Second International Conference on Knowledge Discovery and Data Mining*. AAAI Press, 1996, p. 226–231.

[21] M. A. Branch, T. F. Coleman, and Y. Li, "A subspace, interior, and conjugate gradient method for large-scale bound-constrained minimization problems," *SIAM Journal on Scientific Computing*, vol. 21, no. 1, pp. 1–23, 1999.